Journal of Materials Chemistry C

ROYAL SOCIETY OF CHEMISTRY

PAPER

View Article Online
View Journal | View Issue

Cite this: J. Mater. Chem. C, 2024, 12, 1507

Efficient inverted perovskite solar cells with a low-temperature processed NiO_x/SAM hole transport layer†

Yi Guo, [ab] Like Huang,*[b] Chaofeng Wang,[b] Jiajia Huang,[b] Shuang Liu,[b] Xiaohui Liu, [b] Jing Zhang,[b] Ziyang Hu [b] and Yuejin Zhu*[a]

Nowadays, the inverted (p–i–n) perovskite solar cells have gained increasing attention, especially with the emergence of self-assembled molecules (SAMs) such as MeO-2PACz, 2PACz, CbzPh, *etc.* The SAMs feature a simple preparation process and manifold substrate compatibility, and the electrical characteristics of the attached surface can be well regulated, which is of great significance for improving the device performance. Although there have been many studies about SAMs, some problems still exist. For example, there is a common problem of discontinuities (pinholes) in SAM, which can lead to severe interface recombination. Many SAMs have been proven to be p-type semiconductor materials that can be used as hole transport layers (HTLs). However, it is not yet known whether such a thin molecular film can effectively extract holes and block electrons, as both electrons and holes may tunnel through it. Here, we investigate the roles of MeO-2PACz in improving device performance. Afterwards, a thin NiO_x layer prepared at low temperature (120 °C) is introduced to improve the coverage of the MeO-2PACz SAM layer to further optimize the energy level alignment and passivate defects at the perovskite bottom interface. As a result, the power conversion efficiency (PCE) of the champion device approaches ~22% with a high fill factor (FF) of 83.9%. Furthermore, the ITO/NiO_x/SAM device can maintain 82% of its initial PCE after storing in the ambient air at 25 °C with RH of 20–30% for 800 h.

Received 5th October 2023,
Accepted 7th December 2023

DOI: 10.1039/d3tc03575a

rsc.li/materials-c

1. Introduction

Perovskite materials have been widely used in solar cells due to their high carrier mobility,[1] long carrier life,[2,3] large optical absorption coefficient,[3] low exciton binding energy,[4] high defect tolerance,[5] simple preparation process, low cost, *etc.* In recent years, the efficiency of single-junction perovskite solar cells (PSCs) has rapidly increased from 3.8%[6] to the certified 26.1%.[7] Among various PSCs with different structures, inverted PSCs with p–i–n structure have received widespread attention due to their simple preparation process, weak hysteresis, no need for high-temperature calcination, and compatibility with stacked devices.[8,9] More importantly, after improving the crystallization of perovskite (PVK),[10–12] passivation defects,[13,14] and implementing interface engineering,[15] the efficiency record of inverted PSCs has been significantly improved, almost comparable to the regular n–i–p structure.

At present, the HTLs for inverted PSCs are mostly PTAA, PEDOT:PSS, NiO_x, SAMs, *etc.*[16,17] SAMs are extremely thin organic interlayers formed through electrostatic or chemical adsorption.[18] They play an important role in energy level adjustment and defect passivation, especially in inverted HTL-free PSCs.[19] In addition, many SAMs also serve as hole transport layers.[20–23] Although SAMs have a simple preparation process and manifold substrate compatibility, and can effectively tune the electrical properties of the surface on which they are attached,[24,25] it generally faces the fatal problem of being not dense (with pinholes or disorder). Studies have shown that the chain length and anchoring groups of SAMs,[26,27] the positions of functional groups of SAMs,[27,28] and the morphology of the attached substrate[26] all contribute to the disorder of the deposited SAMs. Organic SAMs are mostly dissolved in organic solvents such as DMF/DMSO, which means that the solvent of the upper layer of the SAMs can also damage them. The pinholes in SAMs can lead to direct contact between PVK and the substrate, resulting in serious recombination losses and leakage currents. In order to improve the compactness of SAMs, researchers have also done a lot of work. Deng *et al.*[22] and Mishimal *et al.*[29] increased the coverage of SAMs by co-depositing two different SAMs, which also improves interface contact with PVK. Most SAMs

[a] School of Information Engineering, College of Science and Technology, Ningbo University, Ningbo 315300, China. E-mail: zhuyuejin@nbu.edu.cn
[b] Department of Microelectronic Science and Engineering School of Physical Science and Technology, Ningbo University, Fenghua Road 818, Ningbo 315211, China. E-mail: huanglike@nbu.edu.cn

† Electronic supplementary information (ESI) available. See DOI: https://doi.org/10.1039/d3tc03575a

are amphiphilic, and some studies have suggested that they are prone to forming micelle nanoparticles in solution, leading to SAMs being unable to disperse and forming defects (not fully covered) during the growth process.[30,31] Therefore, Liu *et al.* developed a co-solvent strategy (*i.e.* mixing DMF and isopropanol in a certain proportion as the solvent for SAMs) to disassemble the micelles in the processing solution to obtain a compact SAM layer.[31] In addition, constructing devices with a double HTL structure was also an effective strategy.[32]

The substrates adhered by SAMs are mostly metals or metal oxides, such as NiO_x, which is a great ''partner'' with SAM. Firstly, NiO_x is a p-type inorganic semiconductor with a wide bandgap ($>$ 3.2 eV), which has suitable matching energy levels with PVK, and has the advantages of low cost, being readily scalable, high transmittance, stable physical and chemical properties, and low-temperature preparation, *etc.*[15,33] Secondly, the surface of NiO_x prepared at a low temperature usually adsorbs a lot of hydroxyl groups (–OH), which can serve as binding sites for some anchoring groups (–COOH, $-SO_3H$, $-PO(OH)_2$) and can passivate interface defects.[34–36] The SAMs also avoid redox reactions between Ni^{3+} and PVK.[34,37] More importantly, existing literatures have shown that NiO_x can enhance the chemical adsorption of SAMs, improve the compactness and uniformity of SAMs, reduce the direct contact probability between ITO and PVK, and effectively avoid leakage currents.[38–41]

In this work, we used a simple solution spin-coating method to grow MeO-2PACz SAMs on ITO or NiO_x, and its specific function and mechanism in the device are systematically studied. SAMs adsorbed on the surface of ITO, increasing the surface vacuum level of ITO, and effectively increasing the work function (WF) of ITO from 4.31 eV to 4.71 eV. The change in WF greatly promote the extraction of carriers at the ITO/PVK interface, leading to a significant reduction in carrier recombination. However, we found that the efficiency regularity of devices based on ITO modified with MeO-2PACz alone was poor, which may be related to the discontinuity of SAMs. Therefore, we introduce a thin NiO_x layer prepared at low temperature (120 °C) between ITO and the SAM layer, which not only effectively avoids direct contact between ITO and PVK due to the discontinuity (pinholes) of the SAM layer, but also further optimizes energy level alignment, passivates bottom interface defects of PVK, and reduces carrier recombination at the interface. Finally, compared to the ITO/SAM device (19.6%) and the ITO/NiO_x device (18.1%), the highest PCE of 21.7% with a high FF (83.9%) has been achieved on the ITO/NiO_x/SAM device.

2. Results and discussion

In reverse HTL-free devices, direct contact between PVK and electrodes can easily cause serious charge carrier recombination and charge transfer barriers (*i.e.* Schottky barriers), or insufficient carrier extraction, greatly reducing the performance of HTL-free PSCs. Therefore, it was necessary to modify ITO to change its surface electrical properties, such as increasing its WF to eliminate or weaken the Schottky barrier.[42] Here, MeO-2PACz also acts as an interface modification layer to alter the properties of the ITO surface. The MeO-2PACz SAMs were dissolved in anhydrous ethanol, and their solubility is shown in Fig. S2 (ESI†). We found that when the concentration of MeO-2PACz exceeded 2 mg mL^{-1}, even though the MeO-2PACz could be dissolved after ultrasonic treatment, the white flocculent suspended particles appeared quickly. Therefore, we spin coated 0.5–5 mg mL^{-1} SAM solution with ultrasonic treatment on ITO substrates. Fig. S3(a) (ESI†) shows the optimal *J–V* curves for devices based on the ITO modified by MeO-2PACz at different concentrations. The champion device based on the MeO-2PACz (1 mg mL^{-1}) modified ITO had a PCE of 19.6%, an open circuit voltage (V_{oc}) of 1.07 V, a current density (J_{sc}) of 23.2 mA cm^{-2} and a fill factor (FF) of 79.0%. In addition, the conductivity of ITO modified by MeO-2PACz with different concentrations was measured (Fig. S3(b), ESI†). Through conducting a current–voltage (*I–V*) measurement, the slope k (*i.e.* *I/V*) and direct conductivity (δ_0) follow this formula: $k = \delta_0 A d^{-1}$, where A is the effective area of the device and d is the thickness of the film. The results showed that ITO modified with 1 mg mL^{-1} MeO-2PACz solution had the highest conductivity, which can be attributed to the optimization of the energy level alignment. Moreover, we also derived a curve of slope change with concentration (Fig. S3(c), ESI†) and found that its conductivity did not always increase with increasing concentration. Therefore, we modified ITO and ITO/NiO_x substrates with the optimal concentration (1 mg mL^{-1}).

Subsequently, we investigated the effects of MeO-2PACz on the properties of the substrates and perovskite films. The occurrences of P element confirm the successfully adsorption of the MeO-2PACz on both ITO and ITO/NiO_x substrates, respectively (Fig. S4, ESI†). From Fig. S5(a) (ESI†), it had almost no effect on the optical transmittance of ITO and ITO/NiO_x, as the thickness of the SAM layer was very thin. However, the SEM images (Fig. 1(e)–(h)) showed that the perovskite film deposited on the ITO or NiO_x modified by MO-2PACz had slightly larger grains than bare ITO or ITO/NiO_x, which was attributed to the decrease of nucleation density due to the slightly worse wettability (the contact angle test shown in Fig. 1(a)–(d)), and the preferential growth of perovskite induced by MeO-2PACz. In fact, the size of perovskite grains was indeed related to the wettability of the substrate, and spinning perovskite solution on a more hydrophobic substrate tends to obtain a perovskite film with larger grains.[43]

From the enhanced (100) diffraction peaks of the perovskite films (Fig. 1i),[8] the MeO-2PACz SAMs improve the crystallinity of perovskite film. This result was consistent with the SEM image. And the full width at half maximum (FWHM) of the (100) diffraction peaks was taken for comparison (Fig. 1(j) and (k)). The crystal grain size can be calculated using the Scherrer equation as follows: $CS = K\lambda/\omega\cos\theta$, where CS is the average grain size, K (0.89) is Scherrer's constant, λ is the wavelength of the incident X-rays, θ is the diffraction angle and ω is the FWHM.[44,45] The FWHM of the (100) diffraction peaks of films on different substrates were 0.123, 0.094, 0.159, and 0.118° for

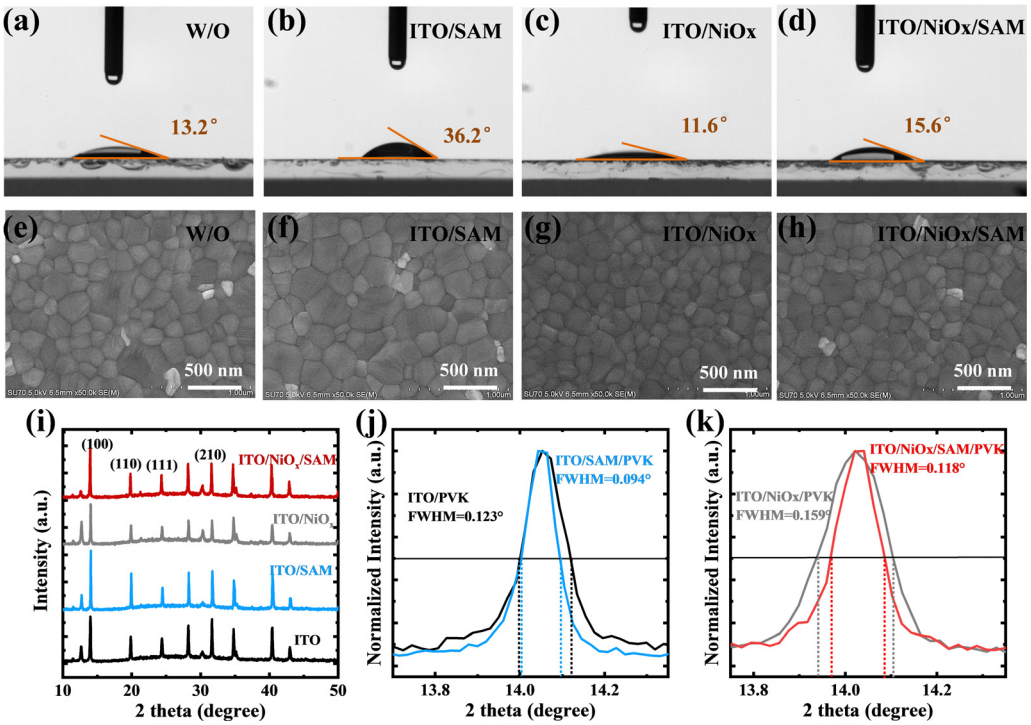

Fig. 1 (a)–(d) The contact angle images of the different substrates. (e)–(h) The SEM images of perovskite films deposited on different substrates. (i) The XRD patterns for different perovskite films. (j) and (k) The full width at half maximum (FWHM) of the (100) plane from XRD of different perovskite films.

bare ITO, ITO/SAM, ITO/NiO_x and ITO/NiO_x/SAM, respectively. The decreased FWHM also indicated that modifying ITO or NiO_x with MeO-2PACz was beneficial for obtaining better perovskite films with larger grains and fewer grain boundaries (GBs). The UV-vis absorption spectra of the different perovskite films were measured (Fig. S5b, ESI†). But no obvious change could be observed, which indicated that although MeO-2PACz improves the crystallization of the perovskite, it does not have a significant impact on the UV absorption of the resulting perovskite films.

The SEM images and XRD patterns showed that the MeO-2PACz can optimize the quality of the perovskite film. However, there was still a problem, the discontinuity (pinhole) of the SAM on bare ITO. The scanning Kelvin probe microscopy (SKPM) images of the ITO and ITO/NiO_x samples before and after the adsorption of MeO-2PACz are shown in Fig. 2(a), (b) and (d), (e). After adsorption, the contact potential difference (CPD) measured by SKPM was found to decrease from −109 to −186 mV for pristine ITO and from −123 to −200 mV for the ITO/NiO_x sample, respectively. From Fig. 2b and e, it was evident that the surface CPD distribution of the ITO/SAM sample was more uneven than that of the ITO/NiO_x/SAM sample. In addition, we used DMF (simulated perovskite solution) to rinse the ITO/SAM and ITO/NiO_x/SAM substrates after MeO-2PACz adsorption and measured the changes in surface CPD (Fig. 2c and f). The ITO/NiO_x/SAM sample had a smaller CPD shift (from −200 to −160 mV) than the ITO/SAM sample (from −186 to −124 mV) after DMF washing, which implied that the NiO_x can promote the adsorption of MeO-2PACz. The potential and height variation diagram along the white line were captured to illustrate its discontinuity (Fig. 2(g) and (h)). From the purple wireframe in Fig. 2g, there was a good correspondence between height and potential. And due to the modification of MeO-2PACz, the surface height and CPD of ITO become more uneven. On the contrary, the surface CPD of ITO/NiO_x samples modified with MeO-2PACz was much more uniform. But the surface roughness (RMS) does not change much because of the high roughness itself (Fig. S6, ESI†). Due to the low roughness of ITO itself, its roughness increased from 2.26 nm to 5.18 nm after spin-coating a discontinuous SAM layer, and decreased from 5.18 nm to 2.50 nm after DMF washing (Fig. S6, ESI†).

Based on the above reasons, we used NiO_x/MeO-2PACz as the HTL (the cross-sectional SEM image is shown in Fig. S7, ESI†). On the one hand, NiO_x can avoid direct contact between ITO and PVK, and enhance the adsorption of MeO-2PACz. On the other hand, MeO-2PACz can passivate defects at the bottom interface of PVK. Fig. 3a is a schematic diagram of the defect passivation effect of MeO-2PACz.

The MeO-2PACz molecules were anchored on the surface of NiO_x through its own phosphate groups (PA) reacting with the hydroxyl groups (–OH) of NiO_x, while also inhibiting the redox reaction between Ni^{3+} and PVK.[37] To demonstrate the binding effect of MeO-2PACz on ITO or NiO_x, the Fourier transform infrared spectroscopy (FTIR) of MeO-2PACz powder and the reflection–absorption infrared spectra (RAIRS) of SAM adsorption on ITO and NiOx were measured (Fig. S8, ESI†). The absorption peaks of P–O (1161.5 cm^{-1}) and P–OH (1025.4 cm^{-1} and 947.5 cm^{-1}) in PA

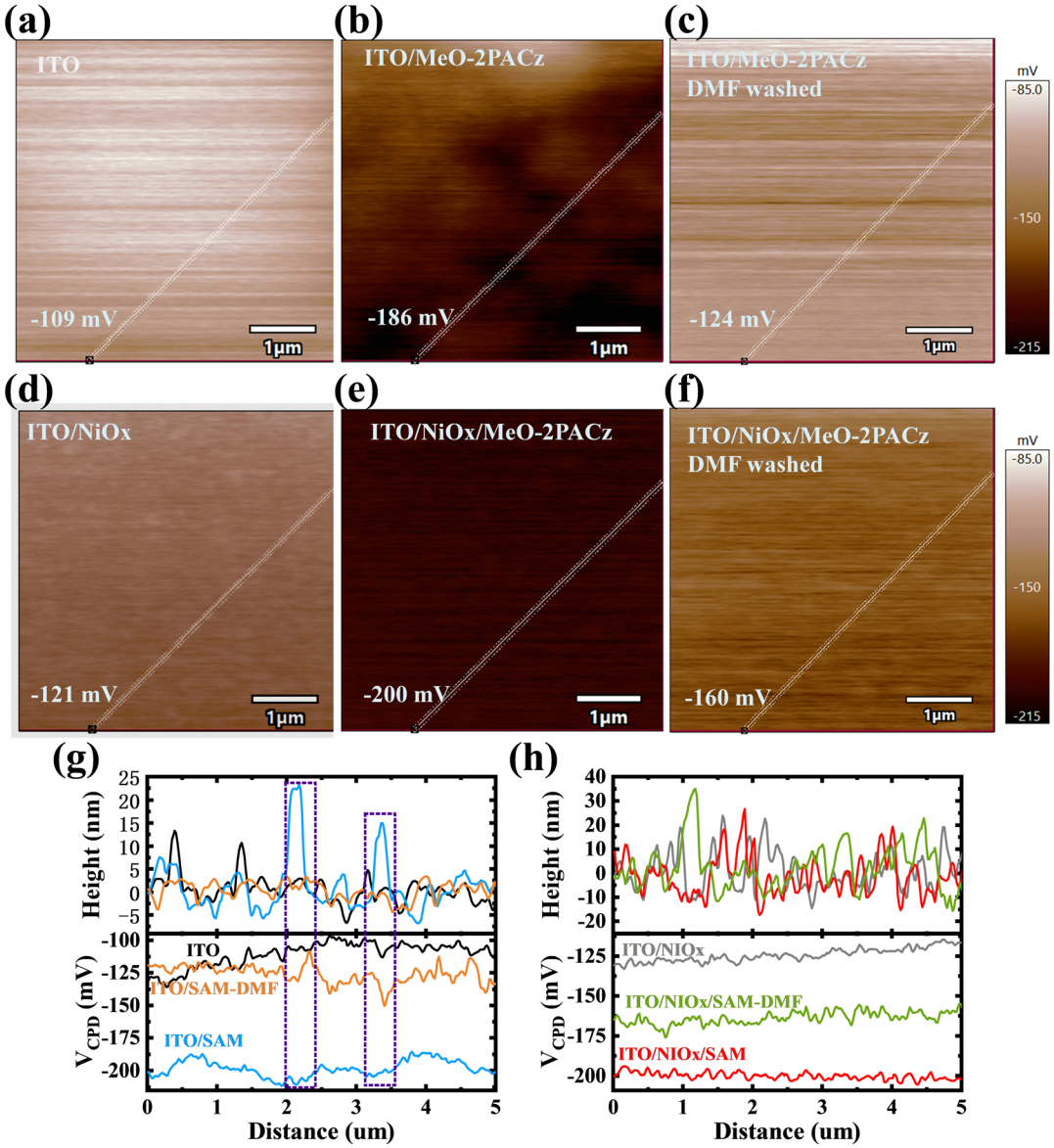

Fig. 2 KPFM images of ITO (a) without and (b) with MeO-2PACz modification, and (c) further washed by DMF. KPFM images of ITO/NiO_x (d) before and (e) after MeO-2PACz modification, and (f) washed by DMF. (g) and (h) The potential and height variation diagram along the white lines on different substrates.

can be used to probe the interaction between MeO-2PACz and oxides.[38]

The shift of the P–OH absorption peak well illustrated the binding effect of PA with hydroxyl groups on the substrate surface (ITO and ITO/NiO_x). The shift of the P═O absorption peak (from 1161.5 to 1162.6 cm^{-1}) was caused by the interaction with Ni^{2+}/Ni^{3+}.[25,38] Therefore, the large number of hydroxyl groups (–OH) on the surface of NiO_x, coupled with the interaction between P═O bonds and Ni^{2+}/Ni^{3+}, makes ITO/NiO_x substrates have stronger adsorption capacity for SAMs. In addition, the solubility of MeO-2PACz in DMF is very high (Fig. S2, ESI†), so we have reason to believe that during the spin-coating of the perovskite solution, some unadsorbed or less firmly adsorbed MeO-2PACz molecules may be dissolved.

They formed Pb–O coordination bonds with uncoordinated Pb^{2+} in the perovskite, thereby passivating defects. To authenticate the potential chemical interaction between PVK and MeO-2PACz, Fourier transform infrared spectroscopy (FTIR) was conducted for PVK powder with MeO-2PACz, as well as for the pure MeO-2PACz powder. The pure MeO-2PACz sample exhibited a characteristic vibration band of the P═O bond at 1161.5 cm^{-1}.[38] Due to the presence of lone pair electrons (*i.e.* Lewis bases) on the O atoms in the P═O bonds, and the uncoordinated Pb^{2+} acting as Lewis acids, they are prone to form coordination bonds (P═O–Pb), leading to a shift of its stretching vibration peak (from 1161.5 to 1159.7 cm^{-1}) (Fig. 3b). The obvious shift of P═O vibration peak suggested a chemical interaction between MeO-2PACz and PVK.

The XPS spectra of Pb 4f for the perovskite films with or without MeO-2PACz modification were measured. From Fig. 3c, a shift of 0.30 eV (from 138.42 to 138.12 eV) has been observed

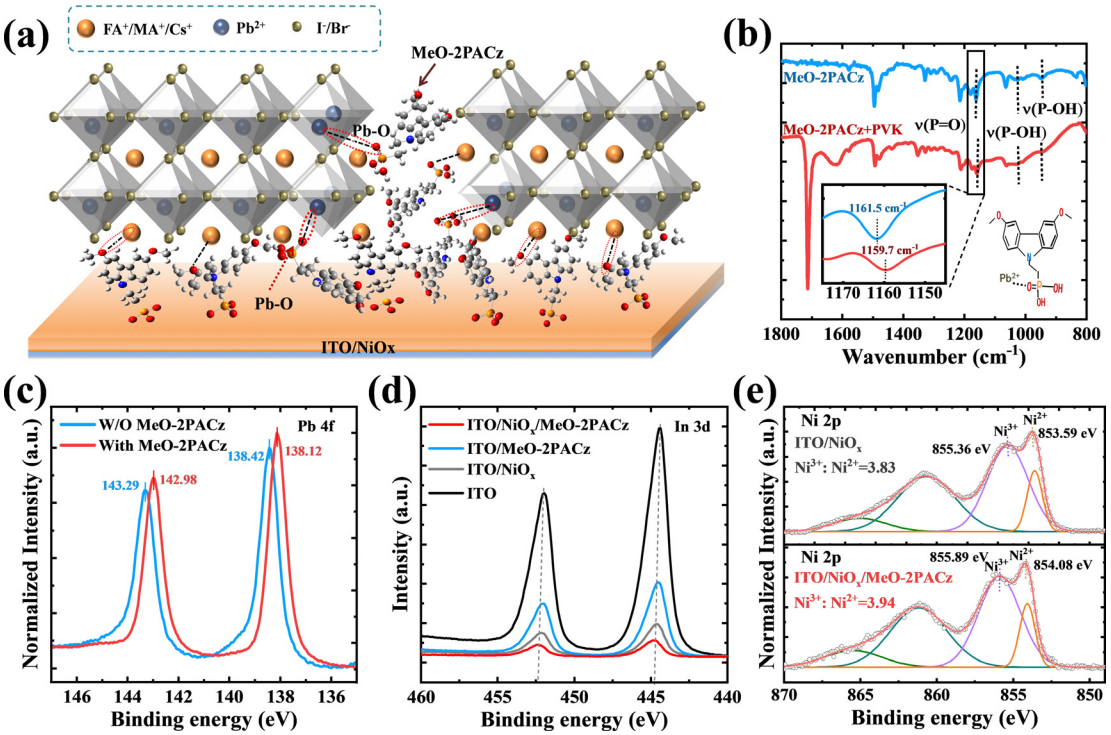

Fig. 3 (a) Schematic diagram of bottom interface defect passivation of PVK by MeO-2PACz molecules anchored on NiO_x. (b) FTIR spectra of MeO-2PACz, and the MeO-2PACz + PbI_2 complex. (c) XPS spectra of Pb 4f for the perovskite films with or without MeO-2PACz modification. The XPS of (d) the In 3d region of ITO and ITO/NiO_x and (e) the Ni 2p region of ITO/NiO_x before and after the adsorption of MeO-2PACz.

for the binding energy (BE) of the Pb $4f_{7/2}$ peak,[46] again confirming the strong coordination of MeO-2PACz with Pb^{2+}. No obvious shift of BE in In 3d can be observed after the adsorption of MeO-2PACz for both the ITO and ITO/NiO_x surfaces (Fig. 3d). However, the BE of the Ni 2p peak for Ni^{2+} positively increased from 853.59 to 854.08 eV after the adsorption (Fig. 3e). This result was consistent with the work of Ye *et al.*[38] This chemical shift also indicated the stronger chemical adsorption between NiO_x and MeO-2PACz. In addition, the increased Ni^{3+}/Ni^{2+} ratio had great impacts on both the conductivity and the energy levels of the corresponding NiO_x films, which were discussed in detail in the following section.

The defect state density of various HTLs has been precisely quantified using the space-charge-limited-current (SCLC) method, as illustrated in Fig. S9 (ESI†). The trap-state density (N_t) is positively correlated with the trap-filling limited voltage (V_{TFL}) (see Note 2 of the Supporting Information). The Nt values were calculated to be 3.92×10^{16}, 2.60×10^{16}, 2.75×10^{16}, and 1.74×10^{16} cm^{-3} for the devices based on bare ITO, ITO/SAM, ITO/NiO_x, and ITO/NiO_x/SAM, respectively. Obviously, devices based on NiO_x/SAM HTL have the lowest defect density. The decreased N_t of the modified devices can be attributed to the defect passivation of MeO-2PACz at the bottom interface of the perovskite.

Compared to ITO/NiO_x or the ITO/SAM substrate, the ITO/NiO_x/SAM substrate has a more favourable energy level alignment with PVK. In order to obtain the energy level structure of each substrate and PVK, the UPS spectra of each substrate and perovskite were measured (Fig. 4a). The band gaps (E_g) of perovskite (~1.57 eV), NiO_x (~3.30 eV), and MeO-2PACz (~3.18 eV) were obtained from their UV-Vis absorbance spectra (Fig. S10, ESI†). From the cut-off edge ($E_{cut\text{-}off}$) of the UPS spectra, the WF of ITO and perovskite were 4.31 eV and 4.23 eV, respectively (WF = 21.2 eV − $E_{cut\text{-}off}$). The distance between the valence band maximum (E_{VBM}) and Fermi level (E_F) of the perovskite is E_f = 1.17 eV (Fig. 4a). Therefore, the conduction band minimum (E_{CBM}) and E_{VBM} of the perovskite are −3.83 eV ($E_g = E_{CBM} - E_{VBM}$) and −5.40 eV ($E_{VBM} = -WF - E_f$), respectively. As shown in Fig. 4b, a concise energy level diagram was drawn. In the absence of a HTL, as the Fermi levels of ITO and PVK were close together, the contact potential was very low, which was insufficient to provide power for the extraction and separation of carriers, resulting in severe carrier recombination at the ITO/PVK interface and a low V_{oc}.[47–49] The WF of ITO increased from 4.31 eV to 4.71 eV after MeO-2PACz modification, thereby improving the carrier transport at the ITO/PVK interface.

It is worth noting that the SAM layer is very thin, which means that both electrons and holes may tunnel through it.[38] Therefore, its blocking effect on electrons mainly comes from the potential generated after contact. Therefore, even though some reports have pointed out that it is an HTL,[17,50] and indeed a P-type semiconductor material in terms of its band structure and bandgap (Fig. S10, ESI†), we believe that the role of MeO-2PACz is more as an interface modification layer in here. After introducing the NiO_x HTL, the high E_{CBM} position of NiO_x

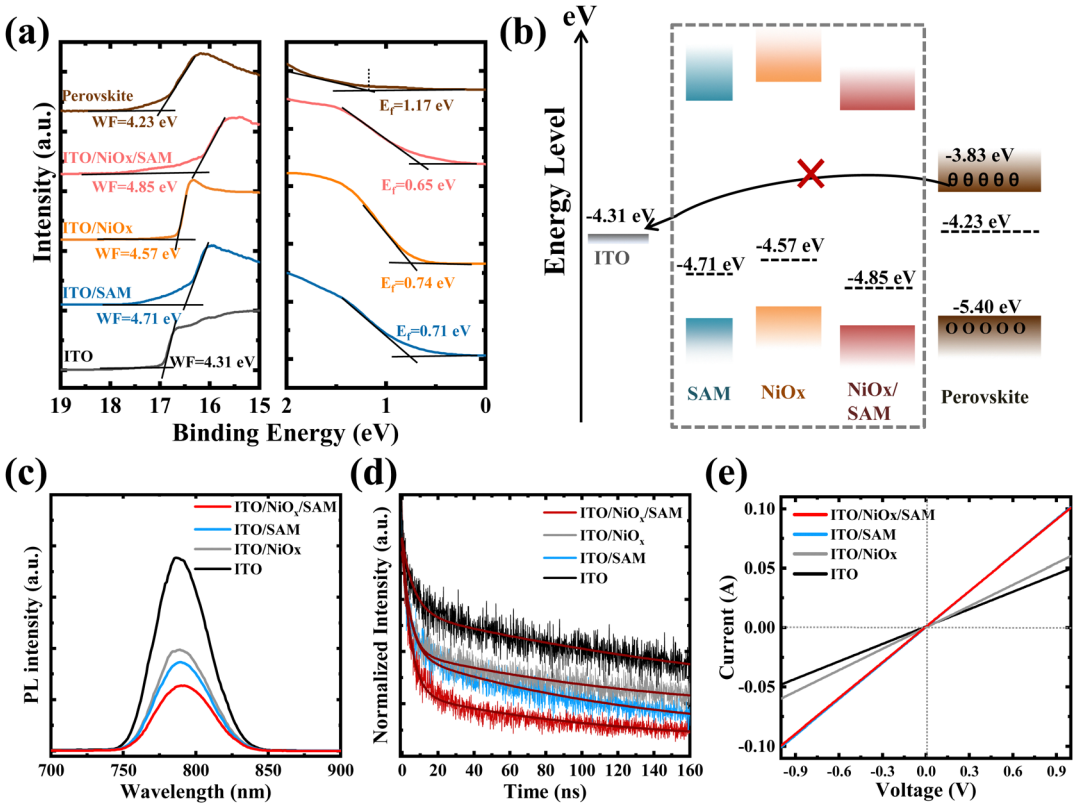

Fig. 4 (a) UPS spectra of the ITO, ITO/SAM, ITO/NiO_x, ITO/NiO_x/SAM and perovskite. (b) Energy level diagram of PSCs. (c) PL and (d) TRPL measurement results of the perovskite films on the different substrates. (e) DC conductivity of the ITO, ITO/SAM, ITO/NiO_x and ITO/NiO_x/SAM films.

can effectively block electron transfer to the positive electrode. The WF of NiO_x increased from 4.57 eV to 4.85 eV after MeO-2PACz modification, optimizing the energy level alignment, promoting carrier transport, and more importantly, reducing interface carrier recombination. In order to research the influences of MeO-2PACz on the transport dynamics of the carrier, the steady-state photoluminescence (PL) spectra and normalized time-resolved PL (TRPL) characterization of the perovskite films on different substrates were carried out (Fig. 4c and d). From Fig. 4c, it was clear that the PL emission intensity of the perovskite film on the ITO/NiO_x/SAM substrate was significantly reduced, which was owing to the excited electrons and holes being transported away. As more direct evidence, the TRPL decay rate of the perovskite film on the ITO/NiO_x/SAM substrate was much faster than other samples. The average decay lifetimes of perovskite films on different substrates are shown in Table S1 (ESI†). In addition, due to the optimization of the energy level alignment, the conductivity of the substrate modified by MeO-2PACz was also improved (Fig. 4e).

We built the complete device shown in Fig. 5a and compared its performance with the other three devices based on different substrates. The optimal *J–V* efficiency curve of the four complete devices is shown in Fig. 5b, and their photovoltaic parameters are summarized in Table 1. The box statistical distribution diagram of them (PCE, V_{oc}, J_{sc}, FF) is shown in Fig. S11 (ESI†). In Table 1, the averages of the parameters are the averages of the values inside the "box". As we can see, an increase in both V_{oc} and J_{sc} of the devices based on MeO-2PACz modification was observed. To this end, the external quantum efficiency (EQE) of each device was measured (Fig. 5c). The integrated J_{sc} values obtained from the EQE spectra were 13.47, 22.56, 22.0 and 23.23 mA cm^{-2} for bare ITO, ITO/SAM, ITO/NiO_x, and ITO/NiO_x/SAM, respectively. The increased J_{sc} was attributed to the optimized energy level structure and the improved conductivity of the substrate for the perovskite. The Mott–Schottky characteristics (Fig. 5d) are usually used to evaluate the built-in potential (V_{bi}) of the PSCs.[51] The V_{bi} of the device based on ITO/NiO_x/SAM was 0.90 V, which was higher than that of other devices. The increased V_{bi} benefited from the optimization of energy level alignment, providing a stronger power for the extraction and separation of the carrier, thereby obtaining a higher V_{oc}. Dark current testing can be used to analyze the non-radiative recombination of the devices, and lower dark current means lower non-radiative recombination (Fig. 5e). In electrochemical impedance spectroscopy (EIS), the values of the series resistance (R_s) and recombination resistance (R_{rec}) correspond to the intercept on the Z′ axis and the diameter of the semicircle, respectively. EIS fitting results demonstrated that the device based on the ITO/NiO_x/SAM substrate showed the highest R_{rec} (Fig. 5f), which also means lower charge recombination. The transient photovoltage (TPV) and transient photocurrent (TPC) measurements are used to investigate the charge recombination lifetime and charge

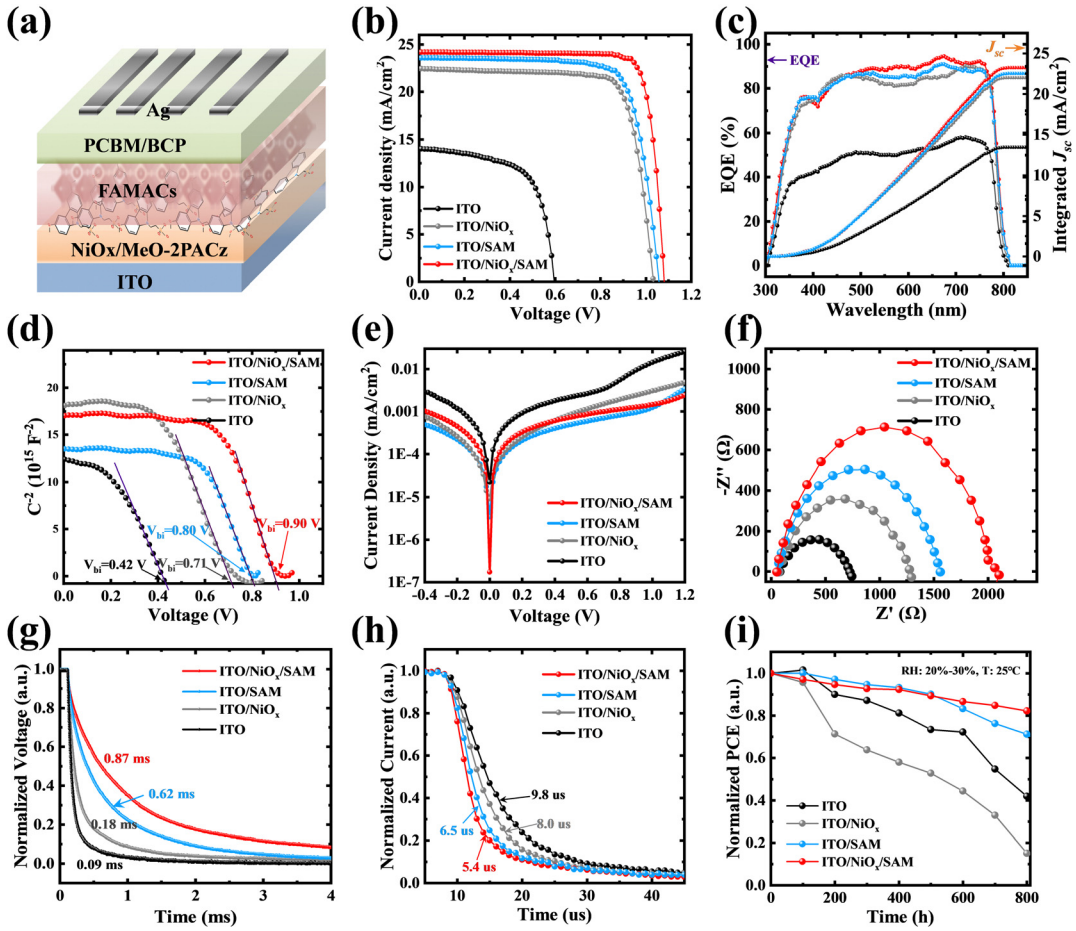

Fig. 5 (a) Device structure diagram based on NiO_x/SAM. (b) *J*–*V* curves and (c) EQE measurement results for four different devices. (d) Dark *J*–*V* measurements of the PSC devices. (e) The transient photovoltage (TPV) decay curve and (f) transient photocurrent (TPC) decay curve. (g) Mott–Schottky analysis. (h) EIS curves of PSC devices. (i) The stability of the devices at 25 °C and RH = 30%.

Table 1 Summary of photovoltaic parameters for the inverted PSCs with four different substrates

Devices		J_{sc} (mA cm^{-2})	V_{oc} (V)	FF (%)	PCE (%)
ITO/PVK	Champion	14.0	0.60	63.8	5.3
	Average	13.1 ± 3.5	0.57 ± 0.07	55.0 ± 8.8	3.8 ± 0.7
ITO/SAM	Champion	23.2	1.07	79.0	19.6
	Average	23.4 ± 0.6	1.06 ± 0.01	77.0 ± 3.4	19.0 ± 2.2
ITO/NiO_x	Champion	22.4	1.04	77.8	18.1
	Average	21.9 ± 0.9	1.03 ± 0.01	77.2 ± 1.5	17.4 ± 0.7
ITO/NiO_x/SAM	Champion	23.9	1.08	83.9	21.7
	Average	23.6 ± 0.8	1.08 ± 0.01	81.3 ± 1.3	20.7 ± 1

extraction time of the PSCs.[52] Fig. 5g and h show the normalized TPV and TPC. It can be observed that a longer charge recombination lifetime and shorter charge extraction time for the ITO/NiO_x/SAM device, which revealed the MeO-2PACz could suppress charge recombination and enhance charge extraction efficiency. Finally, a simple stability test was conducted on four devices. At a relative humidity (RH) of 20–30% and a room temperature of 25 °C, the PCE was tested at regular intervals and the normalized PCE curve was obtained over time (Fig. 5i). The fastest PCE decay of The ITO/NiO_x device was largely caused by the redox reaction at the NiO_x/PVK interface.[37] The stability of the ITO/NiO_x/SAM device is higher than that of the other three devices, which maintain 82% of the initial PCE after storing in the ambient air at 25 °C with RH of 20–30% for 800 h.

3. Conclusions

In summary, we first investigated the effect of MeO-2PACz on inverted HTL-free PSCs. Here, we believe that MeO-2PACz

(SAMs) serve more as an interface modification layer to adjust the energy level alignment. The Fermi energy levels of perovskite and ITO measured by the UPS spectrum are very close, and the potential barrier generated after contact is very low, which is not enough to provide power for carrier extraction and block electron flow, leading to severe carrier recombination at the ITO/PVK interface. The modification of MeO-2PACz raised the WF of ITO from 4.31 eV to 4.71 eV, optimizing the energy level alignment. And the ITO/SAM device achieved a PCE of 19.6% and V_{oc} of 1.07 V. However, from the surface CPD distribution of the ITO/MeO-2PACz substrate, there is indeed discontinuity in the SAM layer. Therefore, we introduce a thin NiO_x layer prepared at low temperature (120 °C) to improve the chemical adsorption of MeO-2PACz SAMs. The WF of the NiO_x substrate modified by MeO-2PACz was increased from 4.57 eV to 4.85 eV, further optimizing the energy level alignment, and the high E_{CBM} position of NiO_x blocked electron flow to the positive electrode. Moreover, MeO-2PACz also passivated the defects at the bottom interface of the perovskite through Pb–O coordination bonds. Finally, devices based on ITO/NiO_x/SAM achieved a champion PCE of 21.7%, a V_{oc} of 1.08 V, a J_{sc} of 23.9 mA cm^{-2} and a high FF of 83.9%. More importantly, the introduction of NiO_x also improves the environmental stability and reverse bias stability of the device. The ITO/NiO_x/SAM device maintains 82% of the initial PCE after storing in the ambient air at 25 °C with RH of 20–30% for 800 h.

Author contributions

Yi Guo: conceptualization, methodology, investigation, data curation, formal analysis, writing – original draft, and writing – review and editing. Like Huang: supervision, writing – review and editing, and project administration. Yuejin Zhu: funding acquisition, supervision. Chaofeng wang: supervision.

Conflicts of interest

There are no conflicts of interest to declare.

Acknowledgements

This work was supported by the National Natural Science Foundation of China (61904182, 62174094) and the K. C. Wong Magna Fund in Ningbo University. L. K. H. would like to express his thanks for the sponsored open project of the National Laboratory of Solid State Microstructures, Nanjing University (M35013).

References

1 C. C. Stoumpos, C. D. Malliakas and M. G. Kanatzidis, *Inorg. Chem.*, 2013, **52**, 9019–9038.
2 D. W. deQuilettes, S. Koch, S. Burke, R. K. Paranji, A. J. Shropshire, M. E. Ziffer and D. S. Ginger, *ACS Energy Lett.*, 2016, **1**, 438–444.
3 Q. Dong, Y. Fang, Y. Shao, P. Mulligan, J. Qiu, L. Cao and J. Huang, *Science*, 2015, **347**, 967–970.
4 V. D'Innocenzo, G. Grancini, M. J. P. Alcocer, A. R. S. Kandada, S. D. Stranks, M. M. Lee, G. Lanzani, H. J. Snaith and A. Petrozza, *Nat. Commun.*, 2014, **5**, 3586.
5 K. X. Steirer, P. Schulz, G. Teeter, V. Stevanovic, M. Yang, K. Zhu and J. J. Berry, *ACS Energy Lett.*, 2016, **1**, 360–366.
6 A. Kojima, K. Teshima, Y. Shirai and T. Miyasaka, *J. Am. Chem. Soc.*, 2009, **131**, 6050–6051.
7 Best Research-Cell Efficiency Chart, *National Renewable Energy Laboratory*, **https://www.nrel.gov/pv/cell-efficiency.html** (accessed October 2023).
8 C. Zhang, X. Shen, M. Chen, Y. Zhao, X. Lin, Z. Qin, Y. Wang and L. Han, *Adv. Energy Mater.*, 2022, **13**, 2203250.
9 M. Zhang, F. Zhang, K. Shi, W. Zhang, J. Huang and H. Qiu, Polymer passivation of defects in inorganic perovskite solar cells, *Optoelectron. Lett.*, 2022, **18**, 338–342.
10 Y. Zheng, X. Wu, J. Liang, Z. Zhang, J. Jiang, J. Wang, Y. Huang, C. Tian, L. Wang, Z. Chen and C.-C. Chen, *Adv. Funct. Mater.*, 2022, **32**, 2200431.
11 R. Dai, X. Meng, J. Zhang, Z. Cai, L. Tan and Y. Chen, *Adv. Funct. Mater.*, 2023, 2305013.
12 X. Shen, B. M. Gallant, P. Holzhey, J. A. Smith, K. A. Elmestekawy, Z. Yuan, P. V. G. M. Rathnayake, S. Bernardi, A. Dasgupta, E. Kasparavicius, T. Malinauskas, P. Caprioglio, O. Shargaieva, Y.-H. Lin, M. M. McCarthy, E. Unger, V. Getautis, A. Widmer-Cooper, L. M. Herz and H. J. Snaith, *Adv. Mater.*, 2023, **35**, 2211742.
13 R. Chen, J. Wang, Z. Liu, F. Ren, S. Liu, J. Zhou, H. Wang, X. Meng, Z. Zhang, X. Guan, W. Liang, P. A. Troshin, Y. Qi, L. Han and W. Chen, *Nat. Energy*, 2023, **8**, 839–849.
14 H. Cheng, C. Liu, J. Zhuang, J. Cao, T. Wang, W.-Y. Wong and F. Yan, *Adv. Funct. Mater.*, 2022, **32**, 2204880.
15 H. Wang, W. Zhang, B. Wang, Z. Yan, C. Chen, Y. Hua, T. Wu, L. Wang, H. Xu and M. Cheng, *Nano Energy*, 2023, **111**, 108363.
16 W. Yan, S. Ye, Y. Li, W. Sun, H. Rao, Z. Liu, Z. Bian and C. Huang, *Adv. Energy Mater.*, 2016, **6**, 1600474.
17 K. Almasabi, X. Zheng, B. Turedi, A. Y. Alsalloum, M. N. Lintangpradipto, J. Yin, L. Gutiérrez-Arzaluz, K. Kotsovos, A. Jamal, I. Gereige, O. F. Mohammed and O. M. Bakr, *ACS Energy Lett.*, 2023, **8**, 950–956.
18 E. Yalcin, M. Can, C. Rodriguez-Seco, E. Aktas, R. Pudi, W. Cambarau, S. Demic and E. Palomares, *Energy Environ. Sci.*, 2019, **12**, 230–237.
19 Z. Chen, Y. Li, Z. Liu, J. Shi, B. Yu, S. Tan, Y. Cui, C. Tan, F. Tian, H. Wu, Y. Luo, D. Li and Q. Meng, *Adv. Energy Mater.*, 2023, **13**, 2202799.
20 W. Wang, K. Wei, L. Yang, J. Deng, J. Zhang and W. Tang, *Mater. Horiz.*, 2023, **10**, 2609–2617.
21 S. N. Afraj, C.-H. Kuan, J.-S. Lin, J.-S. Ni, A. Velusamy, M.-C. Chen and E. W.-G. Diau, *Adv. Funct. Mater.*, 2023, **33**, 2213939.
22 X. Deng, F. Qi, F. Li, S. Wu, F. R. Lin, Z. Zhang, Z. Guan, Z. Yang, C.-S. Lee and A. K. Y. Jen, *Angew. Chem., Int. Ed.*, 2022, **61**, e202203088.

23 W. Jiang, F. Li, M. Li, F. Qi, F. R. Lin and A. K. Y. Jen, *Angew. Chem., Int. Ed.*, 2022, **61**, e202213560.
24 M. L. Sushko and A. L. Shluger, *Adv. Mater.*, 2009, **21**, 1111–1114.
25 P. J. Hotchkiss, S. C. Jones, S. A. Paniagua, A. Sharma, B. Kippelen, N. R. Armstrong and S. R. Marder, *Acc. Chem. Res.*, 2012, **45**, 337–346.
26 M. D. Losego, J. T. Guske, A. Efremenko, J.-P. Maria and S. Franzen, *Langmuir*, 2011, **27**, 11883–11888.
27 S. Y. Kim, S. J. Cho, S. E. Byeon, X. He and H. J. Yoon, *Adv. Energy Mater.*, 2020, **10**, 2002606.
28 E. Aktas, R. Pudi, N. Phung, R. Wenisch, L. Gregori, D. Meggiolaro, M. A. Flatken, F. De Angelis, I. Lauermann, A. Abate and E. Palomares, *ACS Appl. Mater. Interfaces*, 2022, **14**, 17461–17469.
29 R. Mishima, M. Hino, M. Kanematsu, K. Kishimoto, H. Ishibashi, K. Konishi, S. Okamoto, T. Irie, T. Fujimoto, W. Yoshida, H. Uzu, D. Adachi and K. Yamamoto, *Appl. Phys. Express*, 2022, **15**, 076503.
30 A. Ulman, *Chem. Rev.*, 1996, **96**, 1533–1554.
31 M. Liu, L. Bi, W. Jiang, Z. Zeng, S.-W. Tsang, F. R. Lin and A. K. Y. Jen, *Adv. Mater.*, 2023, 2304415.
32 Y. Tan, X. Chang, J.-X. Zhong, W. Feng, M. Yang, T. Tian, L. Gong and W.-Q. Wu, *CCS Chem.*, 2022, **5**, 1802–1814.
33 L. Xu, X. Chen, J. Jin, W. Liu, B. Dong, X. Bai, H. Song and P. Reiss, *Nano Energy*, 2019, **63**, 103860.
34 J. Zhang, J. Yang, R. Dai, W. Sheng, Y. Su, Y. Zhong, X. Li, L. Tan and Y. Chen, *Adv. Energy Mater.*, 2022, **12**, 2103674.
35 C. Zhang, X. Shen, M. Chen, Y. Zhao, X. Lin, Z. Qin, Y. Wang and L. Han, *Adv. Energy Mater.*, 2023, **13**, 2203250.
36 A. R. M. Alghamdi, M. Yanagida, Y. Shirai, G. G. Andersson and K. Miyano, *ACS Omega*, 2022, **7**, 12147–12157.
37 C. C. Boyd, R. C. Shallcross, T. Moot, R. Kerner, L. Bertoluzzi, A. Onno, S. Kavadiya, C. Chosy, E. J. Wolf, J. Werner, J. A. Raiford, C. de Paula, A. F. Palmstrom, Z. J. Yu, J. J. Berry, S. F. Bent, Z. C. Holman, J. M. Luther, E. L. Ratcliff, N. R. Armstrong and M. D. McGehee, *Joule*, 2020, **4**, 1759–1775.
38 J. Sun, C. Shou, J. Sun, X. Wang, Z. Yang, Y. Chen, J. Wu, W. Yang, H. Long, Z. Ying, X. Yang, J. Sheng, B. Yan and J. Ye, *Sol. RRL*, 2021, **5**, 2100663.
39 N. Phung, M. Verheijen, A. Todinova, K. Datta, M. Verhage, A. Al-Ashouri, H. Köbler, X. Li, A. Abate, S. Albrecht and M. Creatore, *ACS Appl. Mater. Interfaces*, 2022, **14**, 2166–2176.
40 L. Mao, T. Yang, H. Zhang, J. Shi, Y. Hu, P. Zeng, F. Li, J. Gong, X. Fang, Y. Sun, X. Liu, J. Du, A. Han, L. Zhang, W. Liu, F. Meng, X. Cui, Z. Liu and M. Liu, *Adv. Mater.*, 2022, **34**, 2206193.
41 Z. Li, X. Sun, X. Zheng, B. Li, D. Gao, S. Zhang, X. Wu, S. Li, J. Gong, J. M. Luther, Z. A. Li and Z. Zhu, *Science*, 2023, **382**, 284–289.
42 W. Kong, W. Li, C. Liu, H. Liu, J. Miao, W. Wang, S. Chen, M. Hu, D. Li, A. Amini, S. Yang, J. Wang, B. Xu and C. Cheng, *ACS Nano*, 2019, **13**, 1625–1634.
43 C. Bi, Q. Wang, Y. Shao, Y. Yuan, Z. Xiao and J. Huang, *Nat. Commun.*, 2015, **6**, 7747.
44 K. Nakamura, M. Hirata and K. Yokota, *Jpn. J. Appl. Phys.*, 2005, **44**, 701.
45 Z. Dai, J. Xiong, W. Liu, N. Liu, J. Dai, Y. Huang, S. Zhang, Q. Song, Z. Zhang, W. Liang, J. Zhang, Q. Dai and J. Zhang, *ACS Appl. Energy Mater.*, 2022, **5**, 4448–4460.
46 X. Chang, J.-X. Zhong, G. Yang, Y. Tan, L. Gong, X. Ni, Y. Ji, Y. Li, G. Zhang, Y. Zheng, Y. Shao, J. Zhou, Z. Yang, L. Wang and W.-Q. Wu, *Sci. Bull.*, 2023, **68**, 1271–1282.
47 P. Lopez-Varo, J. A. Jiménez-Tejada, M. García-Rosell, S. Ravishankar, G. Garcia-Belmonte, J. Bisquert and O. Almora, *Adv. Energy Mater.*, 2018, **8**, 1702772.
48 L. Huang and Z. Ge, *Adv. Energy Mater.*, 2019, **9**, 1900248.
49 Y. Guo, L. Huang, C. Wang, S. Liu, J. Huang, X. Liu, J. Zhang, Z. Hu and Y. Zhu, *Small Methods*, 2023, **7**, 2300377.
50 H. Liu, J. Dong, P. Wang, B. Shi, Y. Zhao and X. Zhang, *Adv. Funct. Mater.*, 2023, 2303673.
51 O. Almora, C. Aranda, E. Mas-Marzá and G. Garcia-Belmonte, *Appl. Phys. Lett.*, 2016, **109**, 173903.
52 J. Wang, S. Fu, L. Huang, Y. Lu, X. Liu, J. Zhang, Z. Hu and Y. Zhu, *Adv. Energy Mater.*, 2021, **11**, 2102724.